



Published in final edited form as:

Mol Imaging Biol. 2013 December ; 15(6): 776–785. doi:10.1007/s11307-013-0629-8.

Comparison of Standardized Uptake Values in Normal Structures Between PET/CT and PET/ MRI in an Oncology Patient Population

Sharif Kershah¹, Sasan Partovi¹, Bryan J Traughber¹, Raymond F. Muzic Jr.¹, Mark D Schluchter², James K O'Donnell¹, and Peter Faulhaber¹

¹Department of Radiology, University Hospitals Case Medical Center, Case Western Reserve University, 11100 Euclid Avenue, Cleveland, OH, 44106, USA

²Department of Epidemiology and Biostatistics, Case Western Reserve University, 10900 Euclid Avenue, Cleveland, OH, USA

Abstract

Purpose—The purpose of this study was to compare and correlate standardized uptake values (SUV) derived from magnetic resonance attenuation correction (MRAC) with those derived from computed tomography attenuation correction (CTAC) in an oncology patient population.

Procedures—The HIPAA-compliant study was approved by the Internal Review Board and all subjects gave written informed consent prior to inclusion in the study. Forty patients (mean age 61±15.1; 20 male) referred for clinically indicated 2-deoxy-2-[¹⁸F]fluoro-D-glucose (FDG) positron emission tomography/computed tomography (PET/CT) scans also underwent a PET/magnetic resonance imaging (MRI) examination. MRAC was performed using an automatic three-segment model. Regions of interest were drawn over eight normal structures in order to obtain SUV_{max} and SUV_{mean} values. Spearman rank correlation coefficients (*r*) were calculated and two-tailed paired *t* tests were performed to compare the SUV_{max} and SUV_{mean} values obtained from CTAC with those from MRAC.

Results—The mean time after FDG injection was 66±7 min for PET/CT and 117±15 min for PET/MRI examination. MRAC SUV values were significantly lower than the CTAC SUV values in mediastinal blood pool (*p*<0.001 for both SUV_{max} and SUV_{mean}) and liver (*p*=0.01 for SUV_{mean}). The MRAC SUV values were significantly higher in bone marrow (*p*<0.001 for both SUV_{max} and SUV_{mean}), psoas major muscle (*p*<0.001 for SUV_{max}), and left ventricular myocardium (*p*<0.001 for SUV_{max} and *p*=0.01 for SUV_{mean}). For the other normal structures, no significant difference was observed. When comparing SUV values generated from CTAC versus MRAC, high correlations between CTAC and MRAC were observed in myocardium (*r*=0.96/ 0.97 for SUV_{max}/mean), liver (*r*=0.68 for SUV_{max}), bone marrow (*r*=0.80/0.83 for SUV_{max}/mean), lung tissue (*r*=0.70 for SUV_{max}), and mediastinal blood pool (*r*=0.0.68/.069 for SUV_{max}/mean). Moderate correlations were found in lung tissue (*r*=0.67 for SUV mean), liver

Correspondence to: Peter Faulhaber; faulhaber@gmail.com.

Conflict of interest. This study was investigator initiated and was funded by a research grant from Philips. The PET/MRI system was purchased through a State of Ohio Third Frontier Grant.

($r=0.66$ for SUV_{mean}), fat ($r=0.48/0.53$ for SUV_{max/mean}), psoas major muscle ($r=0.54/0.58$ for SUV_{max/mean}), and iliacus muscle ($r=0.41$ for SUV_{max}). Low correlation was found in iliacus muscle ($r=0.32$ for SUV_{mean}).

Conclusions—Using the automatic three-segment model, our study showed high correlation for measurement of SUV values obtained from MRAC compared to those from CTAC, as the reference standard. Differences observed between MRAC and CTAC derived SUV values may be attributed to the time-delay between the PET/CT and PET/MRI scans or biologic clearance of radiotracer. Further studies are required to assess SUV measurements when performing different MR attenuation correction techniques.

Keywords

SUV; PET/CT; PET/MRI; Patient population

Introduction

Dedicated positron emission tomography/magnetic resonance imaging (PET/MRI) continues to gain interest as a powerful new imaging modality with the potential to combine molecular, functional, and anatomical information within one examination [1]. Differences between MRI and computed tomography (CT) that are advantageous in certain applications include MRI's better soft tissue contrast, lack of ionizing radiation, and the ability to perform functional and multi-parametric imaging [2]. Clinical validation of the first PET/MRI systems are currently underway [3] and preliminary case series have recently been published including whole-body oncologic imaging [4, 5] and intracranial tumors [6, 7]. Different magnetic resonance (MR)/PET systems are available on the market. The sequential system used in this study consists of a state of the art PET scanner combined with a high-field 3-T MRI. Other manufacturers have systems which enable simultaneous PET and MRI scanning using avalanche photodiodes, instead of photomultiplier tubes, which are located within the MRI gantry [5].

It has been widely established that attenuation correction is necessary for clinical PET imaging and, with the widespread availability of combined PET/CT scanners, CT-based attenuation correction has become the standard approach. Attenuation measurements made with CT, which uses lower energy photons, are used to map the 511-keV photons of the PET images [8, 9]. In comparison, attenuation correction in PET/MRI is more challenging than in PET/CT because signal intensity in MRI depends on the density of hydrogen nuclei, their local environment, and details of the acquisition sequence, as opposed to properties that determine photon attenuation such as atomic number and electron density [10]. A variety of strategies for estimating photon attenuation from MRI data are being considered: (1) segmentation, where tissues are identified and attenuation coefficients assigned based on standard reference values, (2) atlas-based, where images are corrected based on a template data set for which attenuation has been measured, and (3) mapping functions that mathematically transform MRI signal intensities into linear attenuation coefficients [11, 12]. One method for segmentation, attempts to resolve tissue types by using one or more specialized MRI sequences such as ultra-short echo time (UTE), intended to resolve air and

cortical bone, and Dixon, intended to resolve fat and water [13–18]. While these methods have potential, they have not been fully evaluated for clinical use.

In this study, we evaluated a commercially implemented automatic three-segment model for MR-based attenuation correction. This method uses a dedicated T1-weighted MRI sequence followed by an automated image processing technique where the outer contours of the body and lungs are identified using a region-growing technique with threshold analysis [19]. The three segments that are assigned attenuation values are: (1) air outside the patient, (2) lungs, and (3) all other areas of the patient (bone, soft tissue, etc.). Bone is not represented as a separate segment using this MR attenuation method, which may lead to a certain degree of error in standardized uptake values (SUV) calculations. Comparisons were made between SUV derived from MR attenuation correction (MRAC) and CT attenuation correction (CTAC) in patients referred for clinically indicated 2-deoxy-2-[¹⁸F]fluoro-D-glucose (FDG) PET/CT examinations.

Materials and Methods

Patients

Between February 2012 and May 2012, 40 patients (mean age 61; range 29–91; 20 males, 20 females) referred for clinically indicated FDG PET/CT scans (Tables 1 and 2) underwent an additional PET/ MRI examination immediately following their clinical PET/CT (average time between studies 50 min; range 28–80 min). All investigations were performed in a university hospital setting as part of an internal review bo-approved and HIPAA-compliant study. All subjects gave written informed consent prior to undergoing the PET/ MRI scans.

PET/CT

Routine FDG PET/CT was performed with a current-generation, large-bore PET/CT scanner with time of flight capability (Philips Gemini TF PET/CT, Philips Healthcare, Andover, MA) [20] according to a standard clinical protocol. Patients fasted for at least 6 h prior to the study. Following intravenous FDG injection and a period of time for tissue accumulation, PET images were acquired with approximately eight to nine bed positions at 90–120 s per position. CT images for attenuation correction were acquired with routine low-dose protocol (120 kV, 100 mAs, dose modulation, pitch 0.813, slice thickness 5 mm) and without intravenous contrast. The overall imaging time in this study for a diagnostic PET/CT was around 20 min.

PET/MRI

Following the PET/CT procedure, the PET/MR examination was performed as soon as practical. FDG PET/MRI was performed with a combined current-generation PET with time of flight technology and 3.0-T MRI system (Philips Ingenuity TF PET/MR, Philips Healthcare, Andover, MA) [21]. PET images were acquired with eight to nine bed positions at approximately 120–150 s per position. MR images were acquired with four bed positions using an integrated radiofrequency body coil using a multi-station protocol (slab size of 6 cm) with maximum field of view of 46 cm. No MR contrast agents were used in any of the patients. The PET/MRI protocol was based on manufacturer instructions and institutional

protocols. A free-breathing, 3D T1-weighted spoiled gradient echo sequence (TE 2.3 ms, TR 4 ms, 2° flip angle) was acquired. Attenuation correction was performed using a three-segment, atlas-based method [19] implemented in FDA-cleared software provided by the scanner manufacturer. The overall imaging time in this study for a diagnostic PET/MRI was around 30 min.

Image Analysis

Image analysis was performed using commercially available software (MIM Version 5.2, MIM Software Inc., Cleveland, OH). SUV measurements within normal tissue of different organs were compared between the PET images obtained using CTAC and MRAC. The measurements obtained were maximum SUV (SUV_{max}) and mean SUV (SUV_{mean}) where SUVs were normalized by total body weight. Regions of interest (ROI) were drawn in the mediastinal blood pool (MBP; 1.2 cm ROI within right atrium), liver (3.0 cm ROI within right lobe) (see Fig. 1 as a representative instance), bone marrow (1.2 cm ROI centered on L4 vertebral body), psoas major muscle (1.2 cm ROI within left psoas major muscle at the level of the iliac crest), left ventricular myocardium (1.2 cm ROI within the mid left ventricular wall), iliacus muscle (1.2 cm ROI within the right iliacus muscle where it initially comes into contact with the psoas major muscle), lung (1.2 cm ROI within the right lung at the level of the hilum), fat (1.2 cm ROI within the right gluteal subcutaneous fat). Care was taken to measure the same region on both PET studies. The sizes of the ROIs were based roughly on the PET Response Criteria in Solid Tumors (PERCIST) criteria, which defines the background FDG activity through a 3-cm diameter spherical ROI in the right hepatic lobe [22]. ROIs in the other organs were defined to be 1.2 cm in order to produce a 1 cm³-volume spherical ROI, based on the proposed size criteria for measuring pathologic lesions.

Statistical Analysis

The mean and standard deviation of the difference between SUV values for the CTAC and MRAC images were calculated. Spearman rank correlation coefficients were calculated between the CTAC and MRAC SUV values. Interpretation of the Spearman rank correlation coefficients were performed according to previously published criteria: A value 0.35 represents a weak correlation; a value between 0.36 and 0.67 represents a moderate correlation; and a value between 0.68 and 1.0 represents a high correlation, where a value of 0.90 represents a very high correlation [23]. Two-tailed paired *t* tests were performed to look for significant differences between the CTAC and MRAC SUV values.

Results

Patients and Measurement Parameters

All patients tolerated the PET/CT and PET/MRI procedures without noting any unusual discomfort. The baseline characteristics along with the clinical indications for PET/CT and PET/MRI respectively are listed in Tables 1 and 2. The mean injected FDG dose was 12.0±1.8 mCi (range 9.1–15.0 mCi). Mean time after FDG injection performing PET/CT was 66±7 min (range 57–87 min). Mean time after FDG injection for PET/MRI investigation was 117±15 min (range 93–159 min). The mean time between start of PET/CT

and PET/MRI was 50 ± 12 min (range 28–80 min). No significant artifacts were encountered on either the PET/CT or PET/ MRI acquisitions. The automated three-segment model for MR attenuation correction purposes was applied without technical difficulties.

SUV values in CTAC and MRAC

One representative example for ROI placement in the liver, including the corresponding CTAC and MRAC images, is demonstrated in Fig. 1. The mean and standard deviation of the differences between SUV values obtained on the CTAC and MRAC images were calculated (Table 3). The mean and standard deviation of the SUVmax and SUVmean values obtained for each of the eight regions from the CTAC and MRAC images are depicted in Fig. 2. Statistical analysis indicated that MRAC SUV values were significantly lower than the CTAC SUV values in mediastinal blood pool (SUVmax and SUVmean) and liver (SUVmean). The MRAC SUV values were significantly higher than the CTAC SUV values in bone marrow (SUVmax and SUVmean), psoas major muscle (SUVmax), and left ventricular myocardium (SUVmax and SUVmean). Lung, iliacus muscle, and fat showed no significant difference in SUV values between the CTAC and MRAC images.

Correlation Analysis Between CTAC and MRAC SUV Values

The correlation coefficients of the organ tissues are listed in Table 3. Scatterplots showing the correlation between SUVmax and SUVmean values of CTAC and MRAC can be found in Figs. 3 and 4, respectively. Very high correlation was seen in left ventricular myocardium (SUVmax/mean). High correlation was seen in bone marrow (SUVmax/mean), lung tissue (SUVmax), mediastinal blood pool (SUVmax/mean), and liver (SUVmax). Moderate correlation was seen in lung tissue (SUVmean), fat (SUVmax/mean), psoas major muscle (SUVmax/mean), iliacus muscle (SUVmax), and liver (SUVmean). Low correlation was seen in iliacus muscle (SUVmean).

Discussion

The aim of this prospective study was to determine if the SUV values in normal tissue obtained from MRAC are comparable to those in CTAC. A commercially implemented automated three-segment model was used for MRAC as mentioned above. This technique uses an automated method for creating MR attenuation maps out of the image data. A dedicated T1-weighted sequence is used in order to have a short acquisition time and to simplify the segmentation step [19].

Previous research has revealed SUV reproducibility difficulties when evaluating FDG PET/CT studies at different sites with different scanners, where differences of up to 30 % have been detected in phantom models [24]. The PET Core Laboratory of the American College of Radiology Imaging Network emphasized the low accuracy of SUV measurements, and advised careful use of SUV for quantification in patients [25]. However, other groups have shown high reproducibility of SUVmean and SUVmax in malignant tumors when performing repeated measurements with the same scanner [26]. When introducing the PERCIST Criteria, Wahl et al. mentioned the pivotal role of using scanners, which are calibrated and maintained well, including the caveat that all patient PET

examinations should be conducted on similar scanners [22]. Considering these publications, it was an important prerequisite for us to acquire data on scanners with the same technology, thus limiting bias due to PET scanners. To achieve this, we used a PET/CT scanner (Philips Gemini TF PET/CT, Philips Healthcare, Andover, MA) [20] and a PET/ MRI scanner (Philips Ingenuity TF PET/MR, Philips Healthcare, Andover, MA) [21] that both use the same PET technology. To the authors' knowledge, this is one of the first patient studies which compare PET/CT and PET/MRI using current generation PET with time of flight technology.

Another aspect of our prospective study design is the relatively short delay, approximately 50 min, between the beginning of the PET/CT and start of PET/MRI, which is comparable to a recently published study by Drzezga, et al. [5]. Average time between injection and PET/CT was 66 min versus 86 min; and average time between injection and PET/MRI was 117 min versus 140 min when comparing the authors' study to the this same study. This study revealed that a long time span may lead to a drop in SUV values within normal tissue and within lesions [5]. In our experience, it was challenging from a logistical point of view to further reduce the delay between injection and PET/ MRI data acquisition.

The reason for different correlation coefficients in the various normal tissues may be partially explained by the applied attenuation correction techniques [27–29]. A possible reason for the lower correlation of CTAC versus MRAC in the iliacus muscle and the higher correlation in the psoas major muscle is based on the difficulties with bone attenuation correction using MRI. Since the iliacus muscle ROI is located deep within the pelvis and immediately adjacent to the iliac bone, the iliacus muscle was expected to show greater photon attenuation than the psoas major muscle measurement which was performed at the level of the iliac crests, and has much less surrounding bone. This would be accurately corrected for using CTAC, but the MRAC technique used in the study does not separate bone and soft tissue when making the attenuation correction. The three-segment MRAC model for whole-body PET/MR used in the study distinguishes between air (external to the patient), soft tissue and lung. Distinguishing cortical bone as a separate segment has been shown to be important for accurate and reliable MR attenuation correction [17, 18, 27].

The lung revealed moderate correlation between MRAC and CTAC SUV_{mean} values and high correlation between SUV_{max} values. A recent study also showed moderate correlation between SUV_{mean} measurements in lung made using PET/CT and PET/MRI [5]. In the three-segment model, the lung is distinguished as a uniform segment [19]. In reality, the lung is composed of areas with different amounts of air, fluid, and soft tissue. Therefore, attenuation correction should ideally be made on an individual voxel-by-voxel basis, taking into consideration the varying tissue types [30]. One approach to improve attenuation correction in the lung is utilizing a Dixon acquisition, which distinguishes water and fat [15]. In a recently published study, the Dixon-based MRAC method showed comparable anatomic localization and SUV values when compared with conventional PET/CT [31]. In order to help distinguish air and cortical bone, a recently published study used the combination of UTE and Dixon to create a four-class tissue segmentation model, which led to results similar to those obtained from CT attenuation corrections [18].

No significant difference was seen between MRAC and CTAC SUV values in lung and fat, possibly due to the low metabolic activity of both tissue types. The study by Chin et al. showed SUV_{mean} values within gluteal fat decreased over time [32]. The study by Chin et al., showed no change in lung uptake over time [32], while the Cheng et al. study showed decreased lung uptake over time [33]. A study by Drzezga et al. showed SUV_{mean} values in lung lower with PET/MRI than with PET/CT [5].

Within the left ventricular myocardium, CTAC SUV values were lower than MRAC SUV values. This difference may be due to physiologic increased uptake over time, which was demonstrated in a prior study [33]. In the mediastinal blood pool, MRAC SUV values were significantly lower than the CTAC SUV values. This decrease can be attributed to the fact that the PET/MRI was acquired approximately 50 min after the PET/CT and clearance of blood pool activity had occurred. Prior studies have shown that blood pool SUV values decrease over time on PET/CT [32, 33].

When evaluating the bone marrow, the MRAC SUV values were significantly higher than the values in CTAC. This can be explained by the fact that bone marrow is a metabolically active organ containing precursor and mature cells of the different hematological cell lines. Prior studies have shown that bone marrow SUV values increase over time [32, 33]. However, a prior study by Drzezga et al.[5] showed SUV_{mean} values within bone decreased between PET/CT and PET/MR acquisition [5].

Our study demonstrated lower SUV_{max} values in the psoas major muscle on CTAC images compared to MRAC images. SUV_{mean} values in the psoas major muscle and SUV_{max}/mean values in the iliacus muscles were not significantly different. In one prior study, SUV_{mean} within the psoas major muscle increased between 1 and 3 h [32]. In two other studies, SUV values in muscle decreased over time [5, 33]. SUV_{mean} values in the liver were lower on the MRAC images in the authors' study and SUV_{max} values in the liver were unchanged. SUV values within the liver decreased in two other studies [5, 33] and were unchanged over time in a third study [32]. These findings make it difficult to determine if the SUV differences between the CTAC and MRAC images in the authors' study are related to physiologic changes or differences in attenuation correction.

Our prospective PET/MRI study has some limitations. First, PET/MR was acquired after the PET/CT due to ethical concerns. This should be taken into account when comparing SUV values from CTAC with those of MRAC. In particular, it is difficult to determine whether differences in SUVs between MRAC and CTAC images are physiologic or based on differences in the attenuation correction technique. In the current study, some MRAC values were higher, some were lower, and others remained unchanged in comparison to CTAC. These observations suggest that some of the differences in measured SUV measurements may be physiologic, as opposed to a systematic error where all values were either higher or lower on the MRAC-derived data.

Second, we used the previously described three-segment MR attenuation correction model for whole-body PET/MR [19]. Previous studies simulating the digital 4D extended cardiac-torso (XCAT) phantom by applying the Geant4 Application for Tomographic Emission

(GATE) Monte Carlo framework and a model of the Philips Gemini TF came to the conclusion that at least five segments should be taken into account for PET/MR attenuation maps: lung, air, soft tissue, cortical, and spongy bone [27]. Future studies, using combined UTE and Dixon sequences may be helpful in this regard.

Third, FDG uptake in the body is influenced by a variety of factors in the individual patient, including, but not limited to, blood glucose level, body temperature, muscle activity, body weight, and insulin level. These parameters were not controlled in our investigation. But it should be considered that in every day clinical practice, these individual factors are accepted as routine variables regarding FDG uptake.

Conclusions

PET/MRI is a new and promising imaging modality. SUV measurements made with PET/CT are clinically useful. Validation of SUV values obtained from MRAC against those from the reference standard CTAC provides evidence that PET/ MRI may also be helpful in clinical decision-making. The commercially implemented automatic three-segment model for MR-based attenuation correction used in this study revealed very high correlation in left ventricular myocardium (SUVmax/mean). High correlation was seen in bone marrow (SUVmax/mean), lung tissue (SUVmax), mediastinal blood pool (SUVmax/mean), and liver (SUVmax). Moderate correlation was seen in lung tissue (SUVmean), fat (SUVmax/mean), psoas major muscle (SUVmax/mean), iliacus muscle (SUVmax), and liver (SUVmean). Low correlation was seen in iliacus muscle (SUVmean). Most of the difference may be attributed to the time-delay between PET/CT and PET/MRI data collection. Research is on-going regarding new methods for MR-based attenuation correction and further studies will be necessary to validate and demonstrate reliability of SUVs in clinical settings.

Acknowledgments

We would like to thank Patrick Wojtylak, CNMT and Piotr Maniawski, PhD for their technical support.

References

1. Beyer T, Freudenberg L, Czernin J, et al. The future of hybrid imaging—part 3: PET/MR, small-animal imaging and beyond. *Insights into Imaging*. 2011; 2:235–246. [PubMed: 22347950]
2. Partovi S, Schulte AC, Jacobi B, et al. Blood oxygenation level-dependent (BOLD) MRI of human skeletal muscle at 1.5 and 3 T. *J Magn Reson Imaging*. 2012; 35:1227–1232. [PubMed: 22246901]
3. Heiss WD. The potential of PET/MR for brain imaging. *Eur J Nucl Med Mol Imaging*. 2009; 36:105–112.
4. Antoch G, Bockisch A. Combined PET/MRI: a new dimension in whole-body oncology imaging? *Eur J Nucl Med Mol Imaging*. 2009; 36:S113–S120. [PubMed: 19104802]
5. Drzezga A, Souvatzoglou M, Eiber M, et al. First clinical experience with integrated whole-body PET/MR: comparison to PET/ CT in patients with oncologic diagnoses. *J Nucl Med*. 2012; 53:845–855. [PubMed: 22534830]
6. Boss A, Bisdas S, Kolb A, et al. Hybrid PET/MRI of intracranial masses: initial experiences and comparison to PET/CT. *J Nucl Med*. 2010; 51:1198–1205. [PubMed: 20660388]
7. Boss A, Stegger L, Bisdas S, et al. Feasibility of simultaneous PET/MR imaging in the head and upper neck area. *Eur Radiol*. 2011; 21:1439–1446. [PubMed: 21308378]

8. Kinahan PE, Townsend DW, Beyer T, et al. Attenuation correction for a combined 3D PET/CT scanner. *Med Phys.* 1998; 25:2046–2053. [PubMed: 9800714]
9. Kinahan PE, Hasegawa BH, Beyer T. X-ray-based attenuation correction for positron emission tomography/computed tomography scanners. *Semin Nucl Med.* 2003; 33:166–179. [PubMed: 12931319]
10. Zaidi H, Montandon ML, Slosman DO. Attenuation compensation in cerebral 3D PET: effect of the attenuation map on absolute and relative quantitation. *Eur J Nucl Med Mol Imaging.* 2004; 31:52–63. [PubMed: 14574512]
11. Hofmann M, Steinke F, Scheel V, et al. MRI-based attenuation correction for PET/MRI: a novel approach combining pattern recognition and atlas registration. *J Nucl Med.* 2008; 49:1875–1883. [PubMed: 18927326]
12. Zaidi H, Montandon ML, Slosman DO. Magnetic resonance imaging-guided attenuation and scatter corrections in three-dimensional brain positron emission tomography. *Med Phys.* 2003; 30:937–948. [PubMed: 12773003]
13. Hofmann M, Bezrukov I, Mantlik F, et al. MRI-based attenuation correction for whole-body PET/MRI: quantitative evaluation of segmentation- and atlas-based methods. *J Nucl Med.* 2011; 52:1392–1399. [PubMed: 21828115]
14. Zaidi H. Is MR-guided attenuation correction a viable option for dual-modality PET/MR imaging? *Radiology.* 2007; 244:639–642. [PubMed: 17709821]
15. Martinez-Moller A, Souvatzoglou M, Delso G, et al. Tissue classification as a potential approach for attenuation correction in whole-body PET/MRI: evaluation with PET/CT data. *J Nucl Med.* 2009; 50:520–526. [PubMed: 19289430]
16. Ma J, Costelloe CM, Madewell JE, et al. Fast Dixon-based multisequence and multiplanar MRI for whole-body detection of cancer metastases. *J Magn Reson Imaging.* 2009; 29:1154–1162. [PubMed: 19388121]
17. Keereman V, Fierens Y, Broux T, et al. MRI-based attenuation correction for PET/MRI using ultrashort echo time sequences. *J Nucl Med.* 2010; 51:812–818. [PubMed: 20439508]
18. Berker Y, Franke J, Salomon A, et al. MRI-based attenuation correction for hybrid PET/MRI systems: a 4-class tissue segmentation technique using a combined ultrashort-echo-time/Dixon MRI sequence. *J Nucl Med.* 2012; 53:796–804. [PubMed: 22505568]
19. Schulz V, Torres-Espallardo I, Renisch S, et al. Automatic, three-segment, MR-based attenuation correction for whole-body PET/MR data. *Eur J Nucl Med Mol Imaging.* 2011; 38:138–152. [PubMed: 20922522]
20. Surti S, Kuhn A, Werner ME, et al. Performance of Philips Gemini TF PET/CT scanner with special consideration for its time-of-flight imaging capabilities. *J Nucl Med.* 2007; 48:471–480. [PubMed: 17332626]
21. Zaidi H, Ojha N, Morich M, et al. Design and performance evaluation of a whole-body Ingenuity TF PET-MRI system. *Phys Med Biol.* 2011; 56:3091–3106. [PubMed: 21508443]
22. Wahl RL, Jacene H, Kasamon Y, et al. From RECIST to PERCIST: evolving considerations for PET response criteria in solid tumors. *J Nucl Med.* 2009; 50(Suppl 1):122S–150S. [PubMed: 19403881]
23. Taylor R. Interpretation of the correlation coefficient: a basic review. *J Diagn Med Sonography.* 1990; 1:35–39.
24. Westerterp M, Pruim J, Oyen W, et al. Quantification of FDG PET studies using standardised uptake values in multi-centre trials: effects of image reconstruction, resolution and ROI definition parameters. *Eur J Nucl Med Mol Imaging.* 2007; 34:392–404. [PubMed: 17033848]
25. Scheuermann JS, Saffer JR, Karp JS, et al. Qualification of PET scanners for use in multicenter cancer clinical trials: the American College of Radiology Imaging Network experience. *J Nucl Med.* 2009; 50:1187–1193. [PubMed: 19525463]
26. Nahmias C, Wahl LM. Reproducibility of standardized uptake value measurements determined by 18F-FDG PET in malignant tumors. *J Nucl Med.* 2008; 49:1804–1808. [PubMed: 18927325]
27. Keereman V, Holen RV, Mollet P, et al. The effect of errors in segmented attenuation maps on PET quantification. *Med Phys.* 2011; 38:6010–6019. [PubMed: 22047365]

28. Robson MD, Gatehouse PD, Bydder M, et al. Magnetic resonance: an introduction to ultrashort TE (UTE) imaging. *J Comput Assist Tomogr.* 2003; 27:825–846. [PubMed: 14600447]
29. Robson MD, Bydder GM. Clinical ultrashort echo time imaging of bone and other connective tissues. *NMR Biomed.* 2006; 19:765–780. [PubMed: 17075960]
30. Johansson A, Karlsson M, Nyholm T. CT substitute derived from MRI sequences with ultrashort echo time. *Med Phys.* 2011; 38:2708–2714. [PubMed: 21776807]
31. Eiber M, Martinez-Moller A, Souvatzoglou M, et al. Value of a Dixon-based MR/PET attenuation correction sequence for the localization and evaluation of PET-positive lesions. *Eur J Nucl Med Mol Imaging.* 2011; 38:1691–1701. [PubMed: 21688050]
32. Chin BB, Green ED, Turkington TG, et al. Increasing uptake time in FDG-PET: standardized uptake values in normal tissues at 1 versus 3 h. *Mol Imaging Biol.* 2009; 11(2):118–122. [PubMed: 19037614]
33. Cheng G, Alavi A, Lim E, et al. Dynamic changes of FGD uptake and clearance in normal tissues. *Mol Imaging Biol.* 2012.10.1007/s11307-012-0600-0

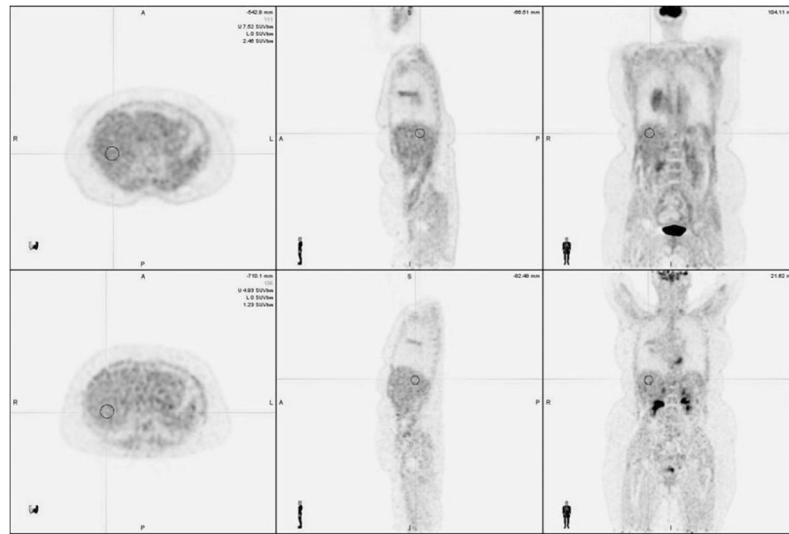


Fig. 1. Sample region of interest (ROI). Representative images of CTAC (*above*) and MRAC (*below*) with demonstrative ROI drawn over the liver.

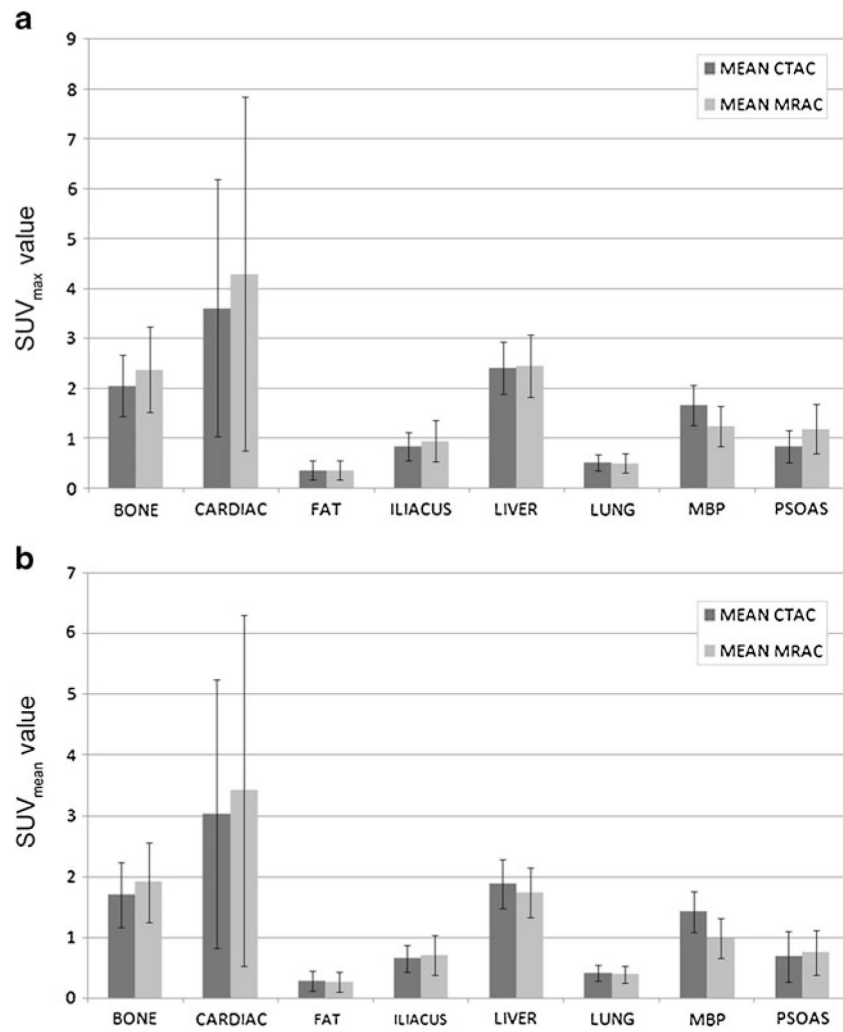


Fig. 2. Mean CTAC and MRAC SUV values are depicted for SUV_{max} (panel a) and SUV_{mean} (panel b) in the various organs. Whiskers depict \pm one standard deviation.

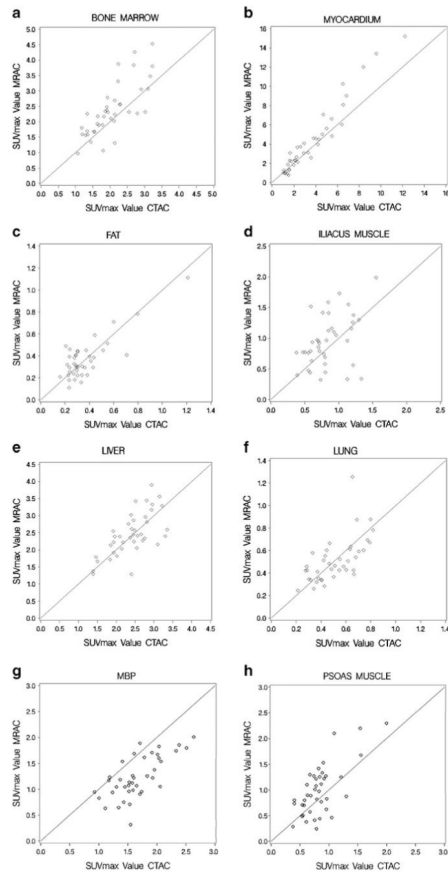


Fig. 3. Scatterplots as a visualization of correlation demonstrating SUVmax values in the different normal structures on the CTAC and MRAC images.

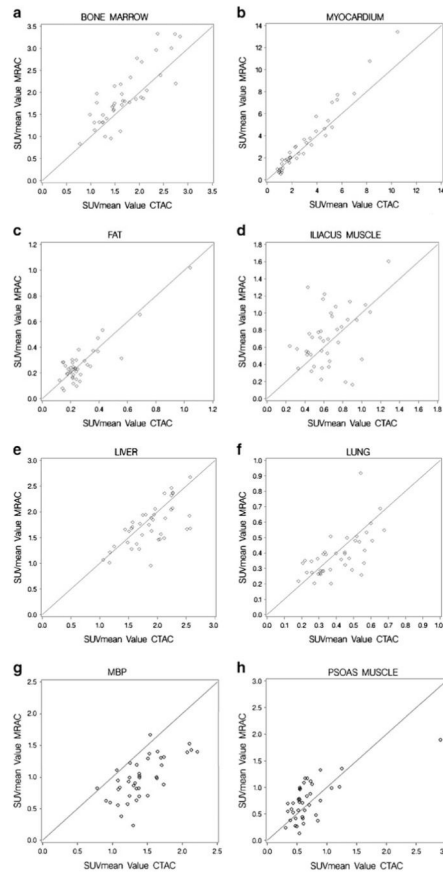


Fig. 4. Scatterplots as a visualization of correlation demonstrating SUVmean values in the different normal structures on the CTAC and MRAC images.

Table 1

Summary of patient baseline characteristics

Age in years, mean±SD (range)	60.6±15.1 (29–91)
Gender, % (<i>n</i>)	
Male	50 (20)
Female	50 (20)
Clinical indication, % (<i>n</i>)	
Breast cancer	5.0 (2)
Colorectal cancer	7.5 (3)
Esophageal cancer	2.5 (1)
H&N cancer	15.0 (6)
Lung cancer	27.5 (11)
Lung nodule	2.5 (1)
Melanoma	10.0 (4)
NHL	25.0 (10)
Pancreatic cancer	2.5 (1)
Vaginal cancer	2.5 (1)

NHL non Hodgkin lymphoma, *H&N* head and neck

Author Manuscript

Author Manuscript

Author Manuscript

Author Manuscript

Table 2
Demographics of each individual patient including height, weight, and calculated BMI

Subject	Age	Sex	Height (ft in)	Weight (lb)	BMI (kg/m ²)	Clinical indication
1	72	F	5' 5"	141	23.5	Lung cancer
2	69	F	5' 5"	175	29.1	Lung cancer
3	71	F	5' 3"	154	27.3	Lung cancer
4	53	M	5' 9"	121	17.9	H&N cancer
5	66	M	5' 11"	150	20.9	Lung cancer
6	85	F	5' 2"	100	18.3	NHL
7	38	F	5' 4"	140	24.0	Breast cancer
8	54	F	5' 5"	147	24.5	Breast cancer
9	83	F	5' 4"	160	27.5	NHL
10	59	M	6' 2"	250	32.1	NHL
11	56	F	5' 3"	185	32.8	NHL
12	73	F	5' 1"	120	22.7	Lung cancer
13	59	F	5' 2"	118	21.6	Lung cancer
14	75	M	5' 7"	140	21.9	Esophageal cancer
15	49	F	5' 3"	140	24.8	Melanoma
16	57	F	5' 5"	208	34.6	Lung cancer
17	91	F	5' 2"	185	33.8	Vaginal cancer
18	36	F	5' 6"	170	27.4	Melanoma
19	67	M	4' 11"	119	24.0	Lung nodule
20	49	F	5' 8"	200	30.4	Lung cancer
21	60	M	5' 6"	151	24.4	Pancreatic cancer
22	46	M	6' 5"	230	27.3	H&N cancer
23	67	M	5' 1"	185	35.0	H&N cancer
24	67	M	5' 8"	111	16.9	H&N cancer
25	68	M	6' 1"	193	25.5	NHL
26	80	M	5' 1"	210	39.7	Melanoma
27	77	F	5' 1"	215	40.6	Lung cancer
28	52	M	6' 1"	185	24.4	H&N cancer

Subject	Age	Sex	Height (ft in)	Weight (lb)	BMI (kg/m ²)	Clinical indication
29	74	M	5' 4"	128	22.0	Lung cancer
30	75	M	5' 5"	140	23.3	Colorectal cancer
31	42	F	5' 4"	228	39.1	Colorectal cancer
32	46	M	5' 5"	160	26.6	NHL
33	63	M	5' 7"	130	20.4	H&N cancer
34	65	F	5' 6"	180	29.1	Lung cancer
35	66	M	6' 0"	176	23.9	NHL
36	39	F	5' 3"	225	39.9	NHL
37	53	M	6' 0"	255	34.6	Melanoma
38	29	M	6' 2"	192	24.7	NHL
39	64	F	5' 4"	215	36.9	Colorectal cancer
40	29	M	6' 4"	160	19.5	NHL

Table 3
SUV measurements in normal structures. Statistical analysis of differences and correlations between CTAC and MRAC

	Bone	Cardiac	Fat	Iliacus	Liver	Lung	MBP	Psoas
SUV _{max}								
Spearman <i>r</i>	0.80	0.96	0.48	0.41	0.68	0.70	0.68	0.54
CTAC	2.06±0.62	3.62±2.58	0.37±0.19	0.84±0.28	2.42±0.52	0.52±0.17	1.67±0.40	0.84±0.33
MRAC	2.38±0.86	4.30±3.54	0.37±0.19	0.95±0.41	2.46±0.62	0.51±0.20	1.24±0.40	1.20±0.49
Difference	0.33±0.55	0.68±1.23	0.01±0.12	0.11±0.39	0.05±0.47	0.00±0.16	-0.43±0.31	0.36±0.29
<i>p</i> value	<0.001	<0.001	0.75	0.09	0.54	0.97	<0.001	<0.001
SUV _{mean}								
Spearman <i>r</i>	0.83	0.97	0.53	0.32	0.66	0.67	0.69	0.58
CTAC	1.70±0.53	3.03±2.21	0.28±0.17	0.65±0.23	1.88±0.40	0.41±0.13	1.42±0.33	0.69±0.42
MRAC	1.91±0.65	3.42±2.88	0.27±0.17	0.71±0.33	1.74±0.41	0.39±0.14	0.98±0.33	0.75±0.36
Difference	0.21±0.36	0.40±0.86	0.00±0.08	0.07±0.32	-0.14±0.33	-0.02±0.12	-0.44±0.27	0.07±0.32
<i>p</i> value	<0.001	0.01	0.72	0.20	0.01	0.24	<0.001	0.20
MBP mediastinal blood pool								

Values reported for CTAC, MRAC, and differences are mean±standard deviation. Difference is MRAC-CTAC difference. All values are rounded to two decimal places